Research Square

Preprints are preliminary reports that have not undergone peer review.
They should not be considered conclusive, used to inform clinical practice,
or referenced by the media as validated information.

Single-Shot Phaseless Electromagnetic Source Imaging in EMC-Relevant Bands Using Frequency-Diverse Metamaterial Apertures

Hamidreza Karami

hamidreza.karami@heig-vd.ch

HES-SO University of Applied Sciences and Arts Western Switzerland

Farhad Rachidi

École Polytechnique Fédérale de Lausanne

Karim Ashouri

École Polytechnique Fédérale de Lausanne

Article

Keywords: Computational electromagnetic imaging, electromagnetic interference, metamaterial aperture, source reconstruction, frequency diversity, phaseless imaging

Posted Date: September 30th, 2026

DOI: https://doi.org/10.21203/rs.3.rs-10839153/v1

License: This work is licensed under a Creative Commons Attribution 4.0 International License.
Read Full License

Additional Declarations: No competing interests reported.

Single-Shot Phaseless Electromagnetic Source Imaging in EMC-Relevant Bands Using Frequency-Diverse Metamaterial Apertures

Hamidreza Karami[1,*], **Farhad Rachidi**[2], **and Karim Ashouri**[3]

[1]School of Engineering and Management Vaud, HES-SO University of Applied Sciences and Arts Western, Switzerland
[2]Electromagnetic Compatibility Laboratory, École Polytechnique Fédérale de Lausanne, Lausanne, Switzerland
[3]Institute of Electrical and Microengineering, École Polytechnique Fédérale de Lausanne, Laboratory for Advanced Electromagnetics and Photonics, Lausanne, Switzerland
[*]hamidreza.karami@heig-vd.ch

ABSTRACT

Accurate localization and reconstruction of electromagnetic interference (EMI) sources remain a critical challenge in electromagnetic compatibility (EMC) diagnostics, particularly in high-density electronic platforms where conventional near-field scanning is slow, mechanically complex, and often reliant on phase-sensitive measurements. In this work, we extend frequency-diverse computational imaging using metamaterial apertures from active reflectivity imaging to passive electromagnetic source reconstruction. A rigorous forward model is derived to relate unknown volumetric current distributions to frequency-domain measurements obtained from a single sensor in a single-shot acquisition. Two metamaterial architectures (a parallel-plate metasurface aperture and a mode-mixing cavity) are redesigned to operate within the EMC-relevant 0.1–6 GHz frequency band and are evaluated numerically. Reconstruction is performed using regularized inversion without assuming sparsity on the source distribution. Both coherent and phaseless imaging scenarios are investigated. Results demonstrate accurate recovery of overlapping Gaussian emitters and complex source distributions under realistic signal-to-noise ratios. The influence of aperture Q-factor, measurement diversity, imaging distance, and number of frequency samples is systematically analyzed. The proposed framework enables rapid, mechanically scan-free, single-sensor electromagnetic source imaging and provides a promising alternative to conventional near-field EMC diagnostic techniques.

Keywords: Computational electromagnetic imaging; electromagnetic interference; metamaterial aperture; source reconstruction; frequency diversity; phaseless imaging

1 Introduction

Continuous increase in operating frequencies and data rates in modern electronic systems has intensified electromagnetic interference (EMI) challenges, particularly in compact and high-density electronic platforms. While advances in high-speed integrated circuits enable aggressive miniaturization, they also intensify parasitic coupling, increase current density, and promote unintended radiation from complex interconnect structures, thereby complicating electromagnetic compatibility (EMC) compliance.

EMI characterization for regulatory compliance is governed by international standards such as CISPR 32[1] and the IEC 61000-6 generic EMC[2,3], which rely primarily on far-field measurements performed in semi-anechoic or reverberation chambers. Although indispensable for certification, these measurements provide only system-level emission information and offer limited spatial resolution, making them unsuitable for localizing individual interference sources on complex PCBs.

Recent antenna-based methods have also localized radiating faults using multi-sensor signal processing[4]. Near-field scanning techniques are widely used for EMI diagnostics and root-cause analysis[5,6], as they enable spatial localization of emission hotspots[7–9]. However, the inherent requirement for point-by-point mechanical scanning imposes a significant temporal overhead and necessitates high-precision positioning hardware, rendering these methods impractical for real-time diagnostics or large-scale inspections[10,11]. Probe loading and mutual coupling effects may also perturb the measured fields if not carefully controlled[12].

Computational imaging with engineered apertures has emerged as an alternative paradigm that enables image formation using reduced measurements and simplified hardware[13–15]. Metamaterial apertures and mode-mixing cavities[16] generate

frequency-diverse field patterns that encode spatial information into spectral measurements, allowing image reconstruction using a single transceiver without mechanical scanning . These approaches have been successfully demonstrated for active coherent object imaging, primarily relying on amplitude- and phase-resolved measurements[14,16]. Related metasurface systems have demonstrated frequency-diverse imaging and joint amplitude-phase encoding for wavefront manipulation[17–19].

Early work on metamaterial apertures exploited resonant subwavelength elements to generate frequency-diverse radiation patterns for compressive coherent imaging, while mode-mixing cavities leveraged wave chaos and multiple internal reflections to enhance measurement diversity at microwave frequencies[20]. More recently, phaseless computational imaging using radiating metasurfaces demonstrated that image reconstruction is feasible even in the absence of phase information, significantly relaxing hardware requirements[21–24].

Despite these advances, existing computational imaging frameworks primarily address active scenarios requiring controlled illumination. Transitioning this paradigm to passive source imaging (where the source is unknown, arbitrary, and potentially non-sparse) remains a formidable challenge for real-world EMI diagnostics.

In this work, we extend metamaterial-based computational imaging from object reconstruction to passive electromagnetic source imaging using a single sensor and a single-shot frequency sweep. A rigorous forward model is developed to relate unknown volumetric current distributions to frequency-domain measurements obtained through a frequency-diverse metamaterial aperture. Unlike conventional reflectivity-based computational imaging, the proposed formulation targets arbitrary radiating sources without assuming sparsity or controlled illumination.

The proposed framework further incorporates intensity-only (phaseless) measurements, reformulating electromagnetic source reconstruction as a generalized phase retrieval problem. This extension significantly relaxes hardware requirements by eliminating the need for phase-coherent receivers, while preserving the frequency-diverse sensing philosophy. To demonstrate feasibility in practical EMC scenarios, two metamaterial aperture architectures (a parallel-plate metasurface aperture and a mode-mixing cavity) are redesigned and numerically validated for operation within the EMC-relevant 0.1–6 GHz band. The effects of aperture Q-factor, modal diversity, frequency-sample density, and imaging distance on reconstruction accuracy are systematically investigated. Together, these developments establish a unified framework for single-sensor, mechanically scan-free electromagnetic source imaging in the EMC frequency range.

The remainder of this paper is organized as follows. Section II presents the forward model for passive electromagnetic source imaging. Section III describes the frequency-diverse metamaterial apertures. Section IV presents numerical source imaging results and analyzes key system parameters. Section V investigates phaseless source imaging. Finally, Section VI concludes the paper.

2 Forward Model for Passive Electromagnetic Source Imaging

In this section, we present an extension of the frequency-diverse metamaterial-aperture framework[13,14] to the imaging of an electromagnetic source distribution. Unlike conventional computational imaging formulations that reconstruct passive reflectivity under controlled illumination, the present formulation targets the reconstruction of unknown radiating sources using a single-port or multi-port metamaterial aperture.

2.1 Continuous Electromagnetic Formulation

The unknown quantity in the problem is a continuous, complex-valued volumetric electric current density distributed over the PCB surface, as shown in Fig. 1.

$$\mathbf{J}(\mathbf{r}_S), \quad \mathbf{r}_S \in V_S \subset \mathbb{R}^3 \tag{1}$$

where V_S denotes a known source region, and $\mathbf{r}_S$ is the source position vector. No sparsity assumption is imposed on the current distribution. For clarity, only impressed electric current densities are considered here. The extension to equivalent magnetic currents is straightforward and follows analogously.

In the frequency domain, the electric field $\mathbf{E}(\mathbf{r})$ generated by the source satisfies

$$\nabla \times \nabla \times \mathbf{E}(\mathbf{r}) - k_0^2 \mathbf{E}(\mathbf{r}) = -j\omega\mu_0 \mathbf{J}(\mathbf{r}) \tag{2}$$

where $k_0 = \omega/c$ is the free-space wavenumber, ω is the angular frequency, c is the speed of light in vacuum, $\mathbf{r}$ is the observation vector, and μ_0 is the permeability of free space. A time dependence of $e^{+j\omega t}$ is assumed.

The radiated electric field can be expressed using the free-space electric dyadic Green's function as

$$\mathbf{E}(\mathbf{r}) = -j\omega\mu_0 \int_{V_S} \overline{\overline{\mathbf{G}}}(\mathbf{r}, \mathbf{r}_S) \cdot \mathbf{J}(\mathbf{r}_S)\, d^3\mathbf{r}_S \tag{3}$$

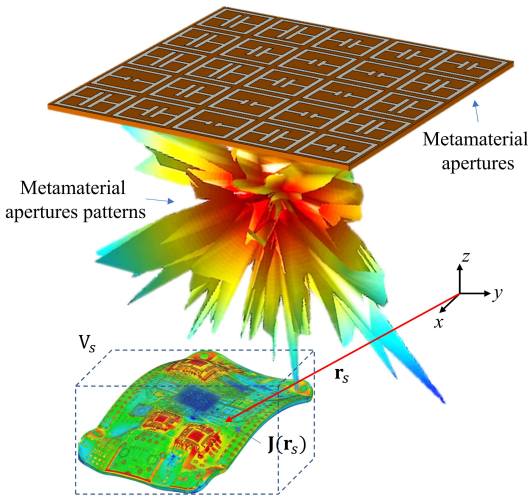


Figure 1. Configuration of the metamaterial aperture and corresponding patterns, along with the continuous complex-valued electric current density defined over the PCB surface.

Let the metamaterial aperture occupy a surface A, where $\mathbf{r}_A = (x_A, y_A, z_A)$ denotes the coordinates of an arbitrary point on the aperture. The metamaterial aperture and its corresponding patterns are also illustrated in Fig. 1. The electric field incident on the metamaterial aperture is therefore

$$\mathbf{E}_A(\mathbf{r}_A) = -j\omega\mu_0 \int_{V_S} \overline{\overline{\mathbf{G}}}(\mathbf{r}_A, \mathbf{r}_S) \cdot \mathbf{J}(\mathbf{r}_S)\, d^3\mathbf{r}_S \tag{4}$$

The complex signal measured at the receive port(s), as shown in Fig. 2, is modeled as

$$g(\omega) = \int_A \mathbf{w}(\mathbf{r}_A, \omega) \cdot \mathbf{E}_A(\mathbf{r}_A)\, d^2\mathbf{r}_A \tag{5}$$

where $\mathbf{w}(\mathbf{r}_A, \omega)$ represents the effective receive weighting function of the metamaterial apertures, incorporating element polarizability, coupling, and feed characteristics. This function effectively maps the incident field to the measured signal at the receiver port(s), analogous to the receiving pattern of the metamaterial apertures. By reciprocity[25], $\mathbf{w}(\mathbf{r}_A, \omega)$ corresponds to the electric field distribution on the aperture generated by unit excitation of the receive port(s).

Substituting the expression for $\mathbf{E}_A$ and interchanging the order of integration yields

$$g(\omega) = \int_{V_S} \mathbf{h}(\mathbf{r}_S, \omega) \cdot \mathbf{J}(\mathbf{r}_S)\, d^3\mathbf{r}_S \tag{6}$$

where the measurement kernel is defined as

$$\mathbf{h}(\mathbf{r}_S, \omega) = -j\omega\mu_0 \int_A \mathbf{w}(\mathbf{r}_A, \omega) \cdot \overline{\overline{\mathbf{G}}}(\mathbf{r}_A, \mathbf{r}_S)\, d^2\mathbf{r}_A \tag{7}$$

Physically, $\mathbf{h}(\mathbf{r}_S, \omega)$ represents the receive-port(s) response to a unit electric dipole located at $\mathbf{r}_S$.

2.2 Discrete Linear Forward Model

Sampling the frequency at ω_k, $k = 1, \ldots, N$, yields the set of measurements

$$g_k = \int_{V_S} \mathbf{h}(\mathbf{r}_S, \omega_k) \cdot \mathbf{J}(\mathbf{r}_S)\, d^3\mathbf{r}_S \tag{8}$$

Discretizing the source region into M voxels V_m, $m = 1, \ldots, M$, and approximating the current density as piecewise constant within each voxel,

$$\mathbf{J}(\mathbf{r}_S) \approx \sum_{m=1}^{M} \mathbf{J}_m \chi_m(\mathbf{r}_S) \tag{9}$$

where $\mathbf{J}_m$ is the current density associated with the mth voxel and $\chi_m(\mathbf{r}_S)$ is the indicator (basis) function defined as

$$\chi_m(\mathbf{r}_S) = \begin{cases} 1, & \mathbf{r}_S \in V_m, \\ 0, & \text{otherwise}, \end{cases} \tag{10}$$

leads to the linear system

$$g_k = \sum_{m=1}^{M} \mathbf{H}_{km} \cdot \mathbf{J}_m \tag{11}$$

with

$$\mathbf{H}_{km} = \int_{V_m} \mathbf{h}(\mathbf{r}_S, \omega_k)\, d^3\mathbf{r}_S \tag{12}$$

Stacking all measurements yields the linear system

$$\mathbf{g} = \mathbf{H}\mathbf{J} \tag{13}$$

where $\mathbf{g} \in \mathbb{C}^N$ is the measurement vector, $\mathbf{J} \in \mathbb{C}^P$ is the vectorized source distribution with $P = 3M$ representing the total number of unknowns (accounting for the three Cartesian components J_x, J_y, and J_z of the current density vector in each voxel), and $\mathbf{H} \in \mathbb{C}^{N\times P}$ is the sensing matrix. Each row of the sensing matrix $\mathbf{H}$ represents a unique spatial transfer function at a specific frequency ω_k. The effectiveness of the reconstruction depends on the mutual coherence of these rows; a frequency-diverse aperture ensures these rows are sufficiently uncorrelated.

In practical measurement scenarios, the recorded data are corrupted by additive measurement noise. The measurement model is therefore more accurately represented as

$$\mathbf{g}_{\mathbf{meas}} = \mathbf{H}\mathbf{J} + \mathbf{n} \tag{14}$$

where $\mathbf{n} \in \mathbb{C}^N$ denotes an additive noise vector. In the numerical examples presented in this paper, white Gaussian noise is added to the simulated data to achieve a prescribed signal-to-noise ratio (SNR). Given noisy complex-valued measurements $\mathbf{g}_{\mathbf{meas}}$, reconstruction is formulated as the regularized inverse problem

$$\hat{\mathbf{J}} = \arg\min_{\mathbf{J}} \|\mathbf{g} - \mathbf{H}\mathbf{J}\|_2^2 + \lambda\, \mathscr{R}(\mathbf{J}) \tag{15}$$

where $\mathscr{R}(\mathbf{J})$ enforces physically motivated priors such as smoothness, energy constraints, or spatial coherence. In this paper, the reconstruction of the vector $\mathbf{J}$ is carried out using Tikhonov regularization. Owing to the ill-conditioned nature of the sensing matrix and the presence of measurement noise[26,27], a regularized least-squares approach is employed to ensure a stable and robust inversion.

This formulation preserves the frequency-diverse measurement philosophy of metamaterial apertures while extending it to passsive, non-sparse source imaging. The forward model is linear in the source current density and does not rely on scattering approximations, enabling applications in passive RF imaging, EMI diagnostics, and electromagnetic source reconstruction.

2.3 Phaseless Source Imaging

We now consider the case where only intensity measurements are available. The measured data are

$$y_k = |g_k|^2 \tag{16}$$

Using the linear forward model, the measurements satisfy

$$y_k = |\langle \mathbf{h}_k, \mathbf{J} \rangle|^2, \qquad k = 1, \ldots, N \tag{17}$$

where $\mathbf{h}_k^T$ denotes the k-th row of $\mathbf{H}$.

Active source reconstruction from intensity-only measurements therefore constitutes a quadratic inverse problem of the form

$$y_k = |\mathbf{h}_k^T \mathbf{J}|^2 \tag{18}$$

which belongs to the class of generalized phase retrieval problems. The solution is unique up to a global phase $e^{j\phi}$, as phase-shifted sources produce identical intensity measurements.

We formulate the phaseless reconstruction as a nonlinear regularized optimization problem

$$\hat{\mathbf{J}} = \arg\min_{\mathbf{J}} \sum_{k=1}^{N} \left(|\mathbf{h}_k^T \mathbf{J}|^2 - y_k\right)^2 + \lambda \mathscr{R}(\mathbf{J}) \tag{19}$$

The regularization term may incorporate spatial support constraints, smoothness priors, or energy bounds consistent with physically admissible current distributions. In the phaseless case, source reconstruction is carried out using a Fienup-type[28] iterative phase retrieval algorithm. Starting from an initial estimate, the algorithm alternates between the measurement and source domains while enforcing consistency with the measured intensity data. At each iteration, the estimated measurements are updated to match the measured amplitudes, and the solution is projected back onto the source domain. The procedure continues until convergence is achieved or a predefined iteration limit is reached.

Frequency diversity of the metamaterial aperture generates a collection of pseudo-orthogonal sensing vectors $\{\mathbf{h}_k\}$ across frequency. When sufficient modal diversity is present and the number of measurements is adequately large relative to the number of unknowns, the sensing matrix exhibits low mutual coherence, enabling stable recovery of the source distribution up to a global phase ambiguity. This formulation establishes a rigorous mathematical framework for phaseless passive electromagnetic source imaging using frequency-diverse metamaterial apertures.

3 Metamaterial Apertures

Metamaterial apertures realize the receive weighting function $\mathbf{w}(\mathbf{r}_A, \omega)$ through frequency-dependent electromagnetic mode diversity. In this work, two metaimagers originally designed for K-band operation (18–26.5 GHz)[14,16,22] are redesigned and numerically simulated for EMC applications within the 0.1–6 GHz band. The geometries used in the original references were also slightly modified to suit this lower frequency range. These apertures serve as representative frequency-diverse platforms to validate the proposed imaging framework. The aperture geometry can certainly be further optimized; however, this optimization is beyond the scope of this study. While many metamaterial apertures in the literature are characterized as transmitting imagers, they are employed here in a purely receiving mode to measure fields from unknown radiating sources. By electromagnetic reciprocity, the frequency-dependent radiation patterns produced under excitation correspond to the receive sensitivity patterns. Under this reciprocal interpretation, the aperture effectively realizes the weighting function $\mathbf{w}(\mathbf{r}_A, \omega)$ defined in Section 2.

3.1 Parallel-Plate Metaimager with Complementary Metamaterial Apertures

The first metaimager architecture consists of a 1.442 m $\times$ 1.442 m parallel-plate waveguide whose top conducting surface is patterned with a 60×60 array of subwavelength resonant metamaterial elements, as shown in Fig. 2. The length of the capacitive loading in each parallel-plate resonant element is randomly varied, producing a spatially disordered distribution of resonance frequencies across the aperture. While originally designed for K-band operation, the geometry and operating parameters have been scaled and adjusted in this work to operate within the 0.1–6 GHz EMC band. One or more feeds are located on the backplane to excite the guided-wave modes within the structure.

The subwavelength elements act as frequency-dependent radiators that exploit the intrinsic dispersion and resonant behavior of the complementary elements to generate spatially and spectrally diverse field patterns as the frequency is swept. Under the principle of electromagnetic reciprocity, these frequency-dependent radiation patterns correspond to frequency-dependent receive sensitivity patterns ($\mathbf{w}(\mathbf{r}_A, \omega)$), allowing the structure to operate as a single-sensor receiver that encodes spatial source information into the frequency domain.

Each complementary metamaterial element is modeled as a polarizable dipole characterized by a frequency-dispersive polarizability tensor

$$\overline{\overline{\alpha}}(\mathbf{r}_A, \omega) = \frac{\alpha_0 \, \omega^2}{\omega_0^2(\mathbf{r}_A) - \omega^2 - j\omega\gamma} \hat{\mathbf{p}}\hat{\mathbf{p}}^T, \tag{20}$$

where $\hat{\mathbf{p}}$ denotes the dipole orientation, $\omega_0(\mathbf{r}_A)$ is the resonance frequency of the element at location $\mathbf{r}_A$, $\gamma = \omega_0/2Q$ is the damping coefficient, and α_0 scales the dipole strength. The resonance frequencies are randomly distributed across the

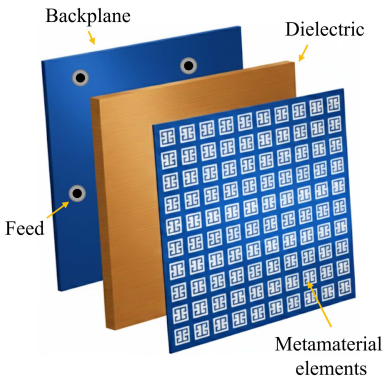


Figure 2. Exploded view of the parallel-plate metaimager with complementary metamaterial apertures, adapted from[14].

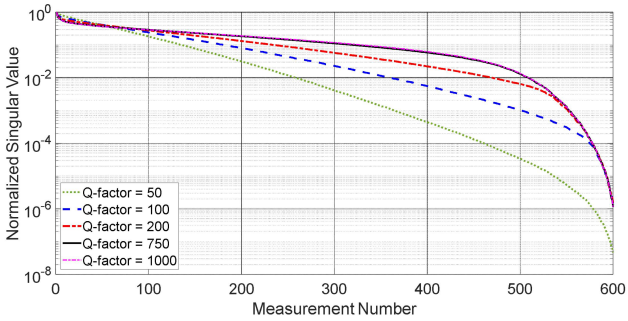


Figure 3. Normalized singular values of the measurement matrix as a function of measurement number for different Q-factors ranging from 50 to 1000.

bandwidth with a quality factor Q of 750. Each complementary metamaterial element is electrically small ($\ll\lambda/10$) over the operating frequency range, so its response is dominated by the fundamental dipolar mode. Higher-order multipoles can therefore be neglected, justifying the dipolar polarizability model in Eq. (20).

The suitability of the resulting sensing matrix ($\mathbf{H}$) is evaluated via the Singular Value Decomposition (SVD) of the measurement modes. As shown in Fig. 3, increasing the Q-factor enhances modal diversity and independence, which stabilizes the inverse problem. However, a saturation point in diversity is observed for Q-factors beyond approximately 750, indicating an upper limit to the information gain from increasing resonator sharpness in this specific aperture geometry. According to Fig. 3, a Q-factor greater than 100 is sufficient for the purpose of source imaging.

The Supplementary Material (SM) further quantifies the modal diversity of the proposed parallel-plate metaimager. Fig. S1 shows the average mutual coherence, μ_g, as a function of the resonator Q-factor, demonstrating that increasing Q reduces inter-mode correlation and enhances frequency diversity[14]. Fig. S2 presents the normalized singular value spectra of the sensing matrix for randomly selected frequencies within the 0.1–6 GHz band, confirming strong diversity and comparable modal richness across frequency samples. Finally, Fig. S3 illustrates the frequency-dependent electric field distributions of the metaimager, highlighting the spatial diversity of the radiated fields that underpins effective source encoding.

In addition to the resonator Q-factor, the number of feed ports also influences the frequency diversity of the metaimager. Multiple ports excite different guided-wave modes within the parallel-plate structure, producing more diverse frequency-dependent field patterns. The SM investigates this effect through mutual-coherence analysis for one to six excitation ports, showing that additional feeds reduce measurement correlation and enhance frequency diversity.

3.2 Mode-Mixing Cavity Metaimager with Random Aperture Distribution on a Uniform Grid

To achieve high modal diversity in a compact footprint, a second metaimager was designed which employs a $650 \times 650 \times 180$ mm^3 rectangular PEC cavity filled with a high-permittivity dielectric ($\varepsilon_r = 11.2$, Rogers RO3010). Enhanced electromagnetic mode-mixing is induced by a 140 mm radius spherical corner perturbation and three strategically placed, rotated dielectric inclusions ($\varepsilon_r = 2.2$ and 6) of varying dimensions. The front face features a randomized distribution of 6 mm circular apertures on a uniform square lattice, excited by a single 50 Ω coaxial probe positioned to ensure multimode excitation from 0.1 to 6 GHz (Fig. 4). Detailed geometrical parameters, material specifications, and frequency-dependent field distributions are

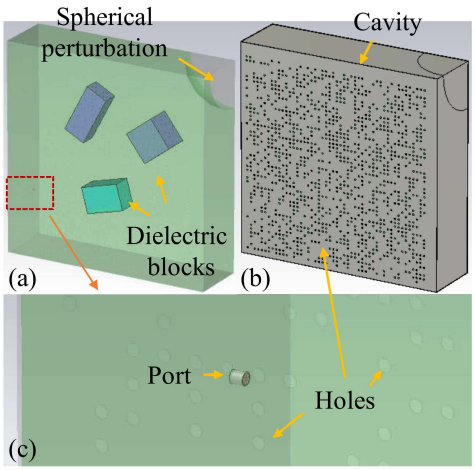


Figure 4. CST-MWS model of the cavity metaimager: (a) interior view, (b) exterior view, and (c) coaxial port configuration. Colored regions denote the dielectric (non-metallic) components inside the cavity.

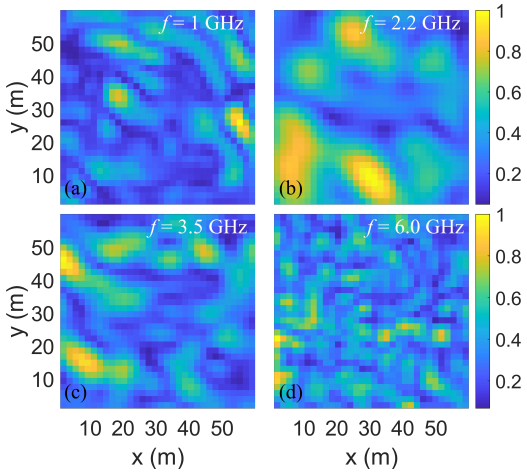


Figure 5. Normalized electric-field magnitude of the mode-mixing cavity Metaimager (Fig. 4) at (a) 1 GHz, (b) 2.2 GHz, (c) 3.5 GHz, and (d) 5.9 GHz.

provided in the SM.

The sensing performance is validated through SVD analysis (detailed in Fig. S4 of the Supplementary Material), which confirms strong modal richness and independence across the operating bandwidth. This frequency-dependent diversity is further visualized in Fig. 5, where the distinct electric-field distributions (computed at $z = 57.5$ cm from the aperture and produced by the system's excitation source) at 1, 2.2, 3.5, and 5.9 GHz demonstrate the system's capacity to generate unique, spatially complex measurement modes. Increasing the number of frequency samples further stabilizes the inverse problem by reducing mutual coherence, thereby enhancing final reconstruction fidelity.

4 Coherent Source Imaging

In this section, we present imaging results obtained with the metaimagers introduced in Section 3 for two different source distributions.

Two approaches are employed to construct the sensing matrix $\mathbf{H}$. For the parallel-plate aperture, $\mathbf{H}$ is formed analytically using the dyadic Green's function together with the modeled frequency-dependent receive weighting function. For the mode-mixing cavity aperture, the frequency-dependent receive sensitivity patterns are extracted from full-wave simulations carried out in CST Microwave Studio, and the sensing matrix is assembled numerically from the simulated field distributions.

In a practical implementation, $\mathbf{H}$ can be obtained through calibration. A small electrically short dipole probe is sequentially positioned at each discretized voxel within the imaging region. For each location, the complex transfer function between the

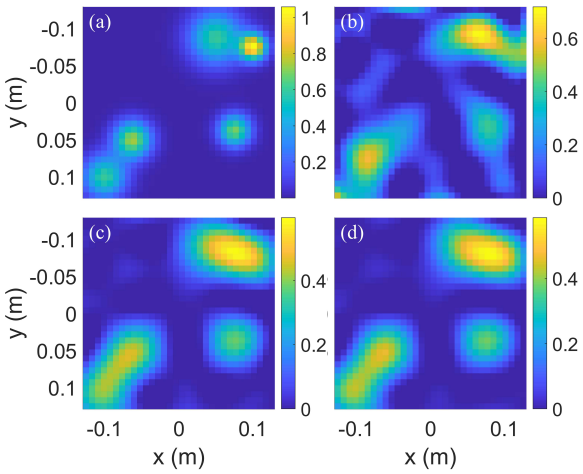


Figure 6. Reconstruction performance of the proposed source imaging method. (a) Original overlapped Gaussian source; reconstructed images at (b) 10 dB SNR, (c) 30 dB SNR, and (d) noiseless condition.

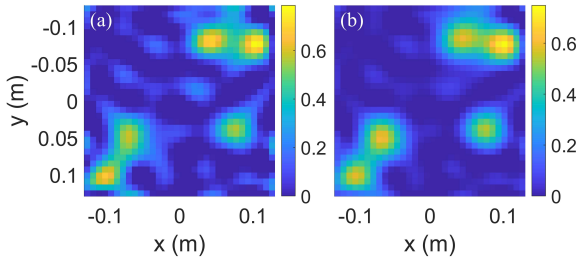


Figure 7. Reconstruction performance of the proposed imaging method for Gaussian sources at a reduced height of 0.25 m (near-field regime). (a) SNR = 10 dB and (b) SNR = 30 dB.

probe (transmit port) and the metamaterial aperture receiver is measured across the operating frequency band using a vector network analyzer. The measured frequency response forms one column of $\mathbf{H}$. Repeating this process for all voxel locations yields the complete sensing matrix, inherently capturing full-wave effects, coupling, and losses of the physical system. This calibration is performed once for a fixed system configuration (aperture geometry, frequency band, and imaging domain). The resulting $\mathbf{H}$ can then be reused for subsequent imaging experiments as long as the system remains unchanged.

Although the theoretical framework supports full vectorial reconstruction of all three Cartesian components of the current density, the numerical results presented here are limited to a single dominant Cartesian component of $\mathbf{J}$. This restriction reduces computational complexity and isolates the impact of frequency diversity on reconstruction performance while preserving the essential physics of the inverse problem.

4.1 Discrete Gaussian Sources Representation with Spatial Overlap

A set of five partially overlapping discrete Gaussian sources is considered to emulate radiation from a PCB, as shown in Fig. 6(a). The PCB is modeled as a 0.25×0.25 m^2 region containing spatially separated Gaussian emitters, with detailed geometrical and amplitude distributions provided in Fig. S5. A parallel-plate–based metaimager (parameters given in Section 3) is used to reconstruct the source distribution. The imaging region spans 0.25×0.25 m^2. The imaging plane is placed 1 m from the source, corresponding to the radiative near-field (Fresnel) region over 1–6 GHz, consistent with the adopted scalar propagation model. The plane is discretized into 32×32 pixels.

Reconstruction results are shown in Fig. 6b, c and d. At an SNR of 10 dB, the reconstruction yields an MSE of 1.03×10^{-2}. Performance improves at higher SNR: 4.02×10^{-3} at 30 dB and 3.88×10^{-3} in the noiseless case, where the recovered images closely match the original distribution. Under practical EMC conditions (typically 15 dB SNR), acceptable performance is achieved, with an MSE of 6.11×10^{-3} (Fig. S6).

The partial interleaving observed between two diagonally separated sources arises from diffraction-limited resolution at increased imaging distance. As the source-to-aperture distance grows, angular resolution degrades according to the aperture-limited bound (approximately $\lambda_{\min}/A$, where A is the surface of the metamaterial aperture.), leading to overlapping reconstructed

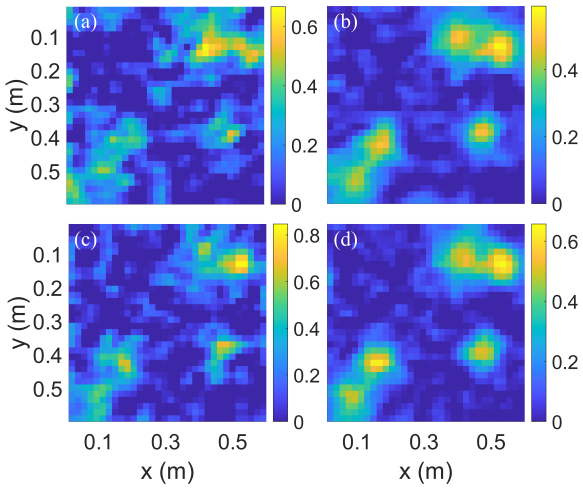


Figure 8. Reconstructed images of discrete Gaussian sources using the mode-mixing cavity metaimager for different SNRs and numbers of measurement modes: (a) 10 dB, 500 modes; (b) 30 dB, 500 modes; (c) 10 dB, 1000 modes; (d) 30 dB, 1000 modes.

profiles. To verify this effect, the metaimager–to-PCB distance is reduced to 0.25 m. As shown in Fig. 7, improved spatial resolution enables clear separation of the Gaussian sources, with MSE values of 5.54×10^{-3} at 10 dB and 1.35×10^{-3} at 30 dB.

The performance of the proposed mode-mixing cavity metaimager is further evaluated for the same source configuration, with a source-to-aperture distance of 0.575 m. Frequency diversity over 1–6 GHz is employed using 500 and 1000 uniformly spaced frequency samples. As shown in Fig. 8(a), reconstruction at an SNR of 10 dB with 500 samples is limited by measurement noise and insufficient modal diversity. Increasing either the SNR or the number of frequency samples improves the image quality, consistent with the measurement-matrix analysis in Section 3, as illustrated in Fig. 8(b)–(c). The best performance is achieved when both parameters are increased simultaneously, as shown in Fig. 8(d).

Although increasing the number of frequency samples enlarges the measurement matrix and computational cost in simulations, this constraint is less restrictive in practical measurements. Modern vector network analyzers can acquire thousands of frequency samples within milliseconds, making dense frequency sampling experimentally feasible.

4.2 Simplified Human Face Source Representation

In this example, a simplified human face is used as the source distribution. Although such a distribution is uncommon in EMC imaging scenarios, it provides a convenient benchmark to evaluate the ability of the proposed method to reconstruct spatially complex features. Binary patterns with sharp spatial transitions are particularly challenging for coherent imaging systems, as abrupt discontinuities contain high spatial-frequency components that are difficult to recover under limited or correlated measurement modes. This example therefore serves to demonstrate the robustness of the proposed frequency-diverse metamaterial aperture in reconstructing scenes with rapid spatial variations.

First, the parallel-plate metaimager shown in Fig. 2 is considered. In contrast to the previous example, the imaging domain is a 0.5×0.5 m^2 located 1 m from the aperture. All structural and electromagnetic parameters remain identical to those defined in Section 3. The assumed binary face target is shown in Fig. 9(a). Reconstructions obtained using the proposed frequency-diverse computational imaging approach with 600 to 12,000 frequency samples at a fixed SNR of 10 dB are presented in Fig. 9(b)–(d). The corresponding MSE values are 1.31×10^{-1}, 5.23×10^{-2}, and 4.9×10^{-2}, respectively. Consistent with the analysis in Section 3, increasing the number of frequency samples reduces the reconstruction error, confirming that additional frequency-diverse measurements significantly enhance imaging performance.

Fig. 10 presents reconstructions of the same face-shaped source obtained using the mode-mixing cavity metaimager shown in Fig. 4, assuming an SNR of 30 dB. The numbers of frequency samples are 500 and 1000 in Fig. 10(a) and (b), respectively. As predicted by the frequency-diversity imaging framework and the conditioning trends discussed in Section 3, increasing the number of frequency samples improves reconstruction quality. In this case, the imaging domain is a 0.65×0.65 m^2 square region. It should be noted that both metaimagers achieve reliable reconstruction performance across the tested scenarios. Their slight differences in behavior arise from the inherent characteristics of their respective architectures.

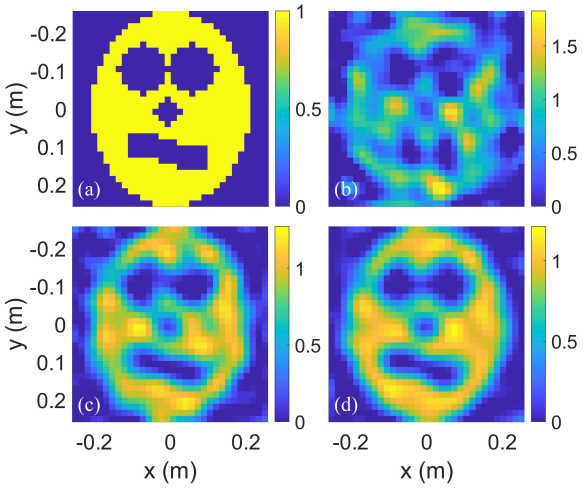


Figure 9. Reconstruction performance of the parallel-plate metaimager for a face-shaped target. (a) Binary face target. (b)–(d) Reconstructions using 600, 3,000, and 12,000 frequency samples at 10 dB SNR.

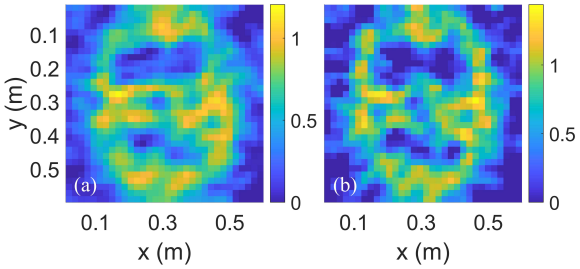


Figure 10. Reconstructed face-shaped source using the mode-mixing cavity metaimager at SNR = 30 dB. (a) 500 frequency samples, (b) 1000 frequency samples.

5 Phaseless Source Imaging

Due to the practical challenges associated with accurate phase measurements in source reconstruction, a phaseless imaging strategy is advantageous. The computational imaging methodology previously introduced in[22,23] for antenna radiation imaging is thus extended here to electromagnetic source reconstruction in the EMC context.

Phaseless inversion belongs to the class of generalized phase retrieval problems, which are inherently non-convex and uniquely recoverable only up to a global phase factor[29,30]. Stable reconstruction generally requires the number of independent measurement modes to exceed by several times the number of unknown parameters, particularly in the absence of sparsity or additional structural priors.

Although the forward model derived in Section 2 is complex-valued, the phaseless measurements consist of real-valued intensity-only data. Accordingly, the inverse problem is reformulated to accommodate this quadratic measurement model. Compared with coherent imaging, phaseless reconstruction requires a larger number of frequency samples to ensure stability. The source plane is discretized into 1024 pixels (32×32), and only the parallel-plate metamaterial aperture (metaimager) is employed to generate frequency-diverse measurement modes.

For the discrete Gaussian example, Figs. 11(a)–(b) show the real and imaginary parts of the true complex source distribution (full specification provided in Fig. S7). The metaimager parameters follow Section 3. The reconstructed real and imaginary components at an SNR of 20 dB are presented in Figs. 11(c)–(d), yielding an MSE of 3.82×10^{-1} for the complex source. Under noiseless conditions, shown in Figs. 11(e)–(f), the MSE decreases to 1.09×10^{-1}.

To further assess performance, the simplified human-face distribution is considered. Figs. 12(a)–(b) illustrate the real and imaginary components of the complex source. The imaging plane is resized to match the physical dimensions of the face model, with a 1 m separation between the metaimager aperture and the source plane. Using intensity-only measurements at an SNR of 30 dB, the reconstructed real and imaginary parts (Figs. 12(c)–(d)) result in an MSE of 2.76×10^{-1}. In the noiseless case, the reconstruction error reduces to 2.18×10^{-1}.

The higher reconstruction error observed in the phaseless case, relative to coherent inversion, arises from the quadratic

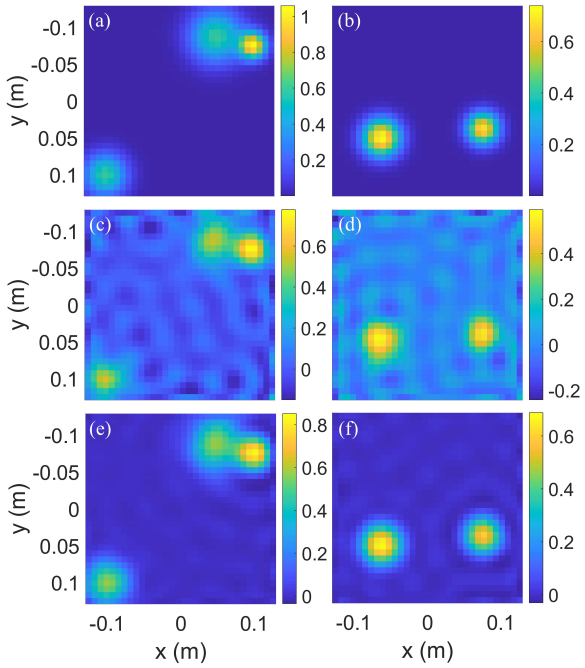


Figure 11. Discrete Gaussian source distribution and phaseless reconstruction results. (a)–(b) Real and imaginary parts of the original source distribution. (c)–(d) Reconstructed real and imaginary parts at SNR = 20 dB. (e)–(f) Reconstructed real and imaginary parts under noiseless conditions.

nonlinearity of the intensity-only measurement model. Unlike the linear coherent formulation, phase retrieval involves solving a non-convex optimization problem that is more sensitive to noise, initialization, and model mismatch. Moreover, the absence of direct phase information reduces the effective information content per measurement, thereby increasing the required measurement diversity for stable recovery.

6 Conclusion

This paper extends frequency-diverse metamaterial-based computational imaging to passive electromagnetic source reconstruction in the EMC frequency band. In contrast to earlier systems based on active illumination and coherent phase-resolved measurements, the proposed framework enables single-shot, single-sensor imaging of unknown radiating sources.

A rigorous forward model was developed to relate volumetric current distributions to frequency-dependent measurements through an effective receive weighting function. Two metamaterial apertures (a parallel-plate metasurface and a mode-mixing cavity) were redesigned and numerically validated at EMC-relevant frequencies. Measurement-matrix analysis verified adequate modal diversity and conditioning for stable inversion.

Numerical simulations demonstrated accurate reconstruction of overlapping Gaussian and complex source distributions under realistic EMC noise conditions. The influence of Q-factor, frequency sampling density, measurement diversity, and imaging distance on reconstruction accuracy was systematically evaluated. Phaseless imaging was shown to be feasible, though it requires a larger number of independent measurement modes and exhibits increased reconstruction error compared to coherent imaging.

Despite the promising numerical results, several limitations should be acknowledged. First, phaseless reconstruction requires a substantially larger number of independent frequency samples compared to coherent imaging. Second, the computational burden increases rapidly with the number of unknowns, which may limit scalability for high-resolution imaging domains. Third, accurate calibration of the frequency-dependent aperture response is essential for experimental implementation.

Overall, the results demonstrate that frequency-diverse metamaterial apertures offer a hardware-efficient alternative to conventional scanning-based EMC diagnostics, enabling reduced mechanical complexity, rapid acquisition, and compatibility with intensity-only measurements. This framework establishes a foundation for cost-effective passive RF imaging, EMI localization, and spectrum-monitoring applications in constrained measurement environments.

Future work will focus on experimental validation and optimized aperture design to reduce measurement redundancy and improve robustness.

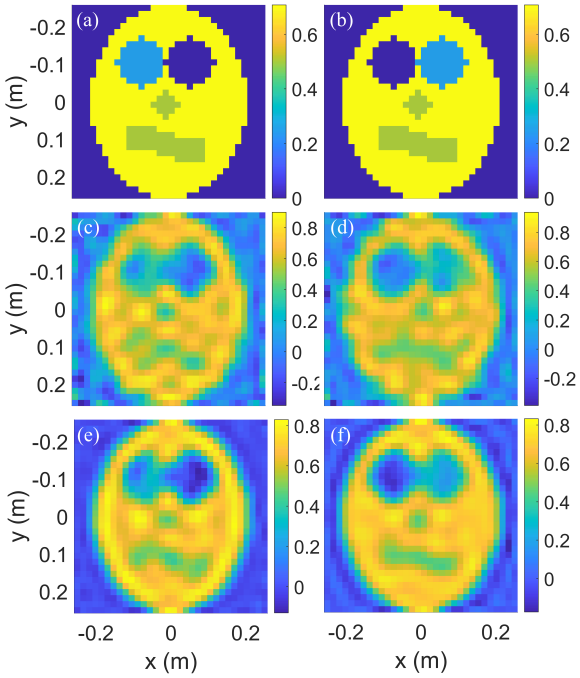


Figure 12. Performance evaluation of the proposed phaseless source imaging method: (a)–(b) original complex source distribution; (c)–(d) reconstruction at 30 dB SNR; (e)–(f) reconstruction under noiseless conditions.

Data Availability

The numerical datasets supporting the findings of this study, including the source distributions, simulated frequency-domain measurements, sensing matrices used for reconstruction, and data underlying the figures, are available from the corresponding author upon reasonable request. CST project files may be subject to software licensing restrictions.

Author Contributions

H.K.: Conceptualisation, Methodology, Software, Formal Analysis, Investigation, Writing – Original Draft, Writing – Review & Editing, Visualisation; F.R.: Conceptualisation, Writing – Review & Editing, Supervision, Project Administration, Funding Acquisition; K.A.: Conceptualisation, Writing – Review & Editing, Supervision.

Funding

No funding was received for this work.

Competing Interests

The authors declare no competing interests.

References

1. International Special Committee on Radio Interference (CISPR), *Electromagnetic compatibility of multimedia equipment – Emission requirements*, CISPR 32:2015, International Electrotechnical Commission (IEC), Geneva, Switzerland, 2015.
2. International Electrotechnical Commission (IEC), *Electromagnetic compatibility (EMC) – Part 6-3: Generic standards – Emission standard for residential, commercial and light-industrial environments*, IEC 61000-6-3:2020, IEC, Geneva, Switzerland, 2020.
3. International Electrotechnical Commission (IEC), *Electromagnetic compatibility (EMC) – Part 6-4: Generic standards – Emission standard for industrial environments*, IEC 61000-6-4:2018, IEC, Geneva, Switzerland, 2018.
4. Amirruddin, M. *et al.* Wavelet-based arcing signal source localization algorithm using a compact multi-square microstrip antenna. *Sci. Rep.* **14**, 22757 (2024). https://doi.org/10.1038/s41598-024-71511-2.

5. E.-X. Liu, W.-J. Zhao, B. Wang, S. Gao and X.-C. Wei, "Near-field scanning and its EMC applications," in *2017 IEEE International Symposium on Electromagnetic Compatibility & Signal/Power Integrity (EMCSI)*, pp. 327–332, IEEE, 2017.

6. X. Su, W. Huang, J. Cho, J. Paek and C. Hwang, "Near field scanning-based EMI radiation root cause analysis in an SSD," in *2023 IEEE Symposium on Electromagnetic Compatibility & Signal/Power Integrity (EMC+ SIPI)*, pp. 202–206, IEEE, 2023.

7. Z. Yan, W. Liu, J. Wang, D. Su, X. Yan and J. Fan, "Noncontact wideband current probes with high sensitivity and spatial resolution for noise location on PCB," *IEEE Transactions on Instrumentation and Measurement*, vol. 67, no. 12, pp. 2881–2891, 2018.

8. Q. Huang, R. Chen, W. Fang, X. Liu, X. Tian, W. Shao, L. Wang *et al.*, "Radiation emission source localization by magnetic near-field mapping along the surface of a large-scale IC with BGA package," *IEEE Transactions on Electromagnetic Compatibility*, vol. 64, no. 2, pp. 495–505, 2022.

9. Z. A. Wang, J. F. Mao, L. J. Jiang and P. Li, "Localization and identification of EMI sources in shielding enclosures based on a two-step source reconstruction method," *IEEE Transactions on Electromagnetic Compatibility*, vol. 65, no. 4, pp. 972–981, 2023.

10. Y.-F. Shu, X.-C. Wei, R. Yang and E.-X. Liu, "An iterative approach for EMI source reconstruction based on phaseless and single-plane near-field scanning," *IEEE Transactions on Electromagnetic Compatibility*, vol. 60, no. 4, pp. 937–944, 2018.

11. H. Rezaei, J. S. Meiguni, M. Soerensen, R. G. Jobava, V. Khilkevich, J. Fan, D. G. Beetner and D. Pommerenke, "Source reconstruction in near-field scanning using inverse MoM for RFI application," *IEEE Transactions on Electromagnetic Compatibility*, vol. 62, no. 4, pp. 1628–1636, 2020.

12. H. He, P. Maheshwari and D. J. Pommerenke, "The development of an EM-field probing system for manual near-field scanning," *IEEE Transactions on Electromagnetic Compatibility*, vol. 58, no. 2, pp. 356–363, 2016.

13. J. Hunt, T. Driscoll, A. Mrozack, G. Lipworth, M. Reynolds, D. Brady and D. R. Smith, "Metamaterial apertures for computational imaging," *Science*, vol. 339, no. 6117, pp. 310–313, 2013.

14. G. Lipworth, A. Mrozack, J. Hunt, D. L. Marks, T. Driscoll, D. Brady and D. R. Smith, "Metamaterial apertures for coherent computational imaging on the physical layer," *Journal of the Optical Society of America A*, vol. 30, no. 8, pp. 1603–1612, 2013.

15. J. N. Mait, G. W. Euliss and R. A. Athale, "Computational imaging," *Advances in Optics and Photonics*, vol. 10, no. 2, pp. 409–483, 2018.

16. T. Fromenteze, O. Yurduseven, M. F. Imani, J. Gollub, C. Decroze, D. Carsenat and D. R. Smith, "Computational imaging using a mode-mixing cavity at microwave frequencies," *Applied Physics Letters*, vol. 106, no. 19, Art. no. 194104, 2015.

17. Gollub, J. N. *et al.* Large metasurface aperture for millimeter wave computational imaging at the human-scale. *Sci. Rep.* **7**, 42650 (2017). https://doi.org/10.1038/srep42650.

18. Cai, C., Li, Y., Li, M., Qin, Y. & Zhou, Y. Phase and amplitude simultaneously coding metasurface with multi-frequency and multifunctional electromagnetic modulations. *Sci. Rep.* **14**, 20904 (2024). https://doi.org/10.1038/s41598-024-72018-6.

19. Ashrafian, M. & Yousefi, L. Subwavelength imaging using orbital angular momentum waves generated by metasurfaces. *Sci. Rep.* **15**, 20539 (2025). https://doi.org/10.1038/s41598-025-04813-8.

20. M. F. Imani, J. N. Gollub, O. Yurduseven, A. V. Diebold, M. Boyarsky, T. Fromenteze, L. Pulido-Mancera, T. Sleasman and D. R. Smith, "Review of metasurface antennas for computational microwave imaging," *IEEE Transactions on Antennas and Propagation*, vol. 68, no. 3, pp. 1860–1875, 2020.

21. M. d'Urso, K. Belkebir, L. Crocco, T. Isernia and A. Litman, "Phaseless imaging with experimental data: facts and challenges," *Journal of the Optical Society of America A*, vol. 25, no. 1, pp. 271–281, 2008.

22. T. Fromenteze, X. Liu, M. Boyarsky, J. Gollub and D. R. Smith, "Phaseless computational imaging with a radiating metasurface," *Optics Express*, vol. 24, no. 15, pp. 16760–16776, 2016.

23. O. Yurduseven, T. Fromenteze, D. L. Marks, J. N. Gollub and D. R. Smith, "Frequency-diverse computational microwave phaseless imaging," *IEEE Antennas and Wireless Propagation Letters*, vol. 16, pp. 2808–2811, 2017.

24. A. V. Diebold, M. F. Imani, T. Sleasman and D. R. Smith, "Phaseless computational ghost imaging at microwave frequencies using a dynamic metasurface aperture," *Applied Optics*, vol. 57, no. 9, pp. 2142–2149, 2018.

25. C. A. Balanis, *Antenna Theory: Analysis and Design*, 4th ed., John Wiley & Sons, Hoboken, NJ, USA, 2016.

26. P. C. Hansen, *Discrete Inverse Problems: Insight and Algorithms*, SIAM, Philadelphia, PA, USA, 2010.

27. D. Colton and R. Kress, *Inverse Acoustic and Electromagnetic Scattering Theory*, 3rd ed., Springer, New York, NY, USA, 2013.

28. J. R. Fienup, "Phase retrieval algorithms: a comparison," *Applied Optics*, vol. 21, no. 15, pp. 2758–2769, 1982.

29. B. Gao, "Affine phase retrieval via second-order methods," *Inverse Problems*, vol. 41, no. 5, p. 055011, 2025.

30. M. Allain, S. Aslan, W. Coene, S. Dirksen, J. Dong, J. Flamant, M. Iwen, F. Krahmer, T. van Leeuwen, O. Melnyk, *et al.*, "Phasebook: a survey of selected open problems in phase retrieval," *Sampling Theory, Signal Processing, and Data Analysis*, vol. 23, no. 2, p. 23, 2025.

Supplementary Files

This is a list of supplementary files associated with this preprint. Click to download.

- SSSIpaperSIv01.docx